

Mechanical properties and microstructure of hemp hurd reinforced polylactide biocomposites for 3D printing

Xianglian Xiao^{1,2}  | Venkata S. Chevali²  | Pingan Song² | Bin Yu³ | Jiabing Feng^{2,4} | Thomas W. Loh⁵ | Hao Wang²

¹School of Materials Science and Engineering, Hunan Institute of Technology, Hengyang, China

²Centre for Future Materials, University of Southern Queensland, Springfield Central, Springfield Central, Australia

³State Key Laboratory of Fire Science, University of Science and Technology of China, Hefei, China

⁴College of Biological, Chemical Science and Engineering, Jiaying University, Jiaying, China

⁵School of Engineering, RMIT University, Melbourne, Australia

Correspondence

Venkata S. Chevali and Hao Wang, Centre for Future Materials, University of Southern Queensland, Springfield Central, QLD 4300, Australia.

Email: venkata.chevali@unisu.edu.au and hao.wang@usq.edu.au

Funding information

Australian Research Council, Grant/Award Numbers: DP230103008, IH220100002; Scientific Research Fund of Hunan Provincial Education Department, Grant/Award Numbers: 21A0569, 23A0632; Forest and Wood Products Australia, Grant/Award Number: PNA360-1516; College Student Innovation and Entrepreneurship Training Program, Grant/Award Number: S202411528190

Abstract

Polylactide (PLA) biocomposite filaments containing hemp hurd (HH) of variable particle size were evaluated in comparison with injection-molded counterparts using single/twin screw extrusion in this study. HH particle size (35, 50, and 160 μm) was parametrically investigated for its efficacy within PLA/HH biocomposites and fused filament fabrication (FFF)-printed parts by assessing its effect on performance through rheological, microstructural, mechanical, and surface finish analyses. In addition, melt flow indexing, rheometry, scanning electron microscopy, mechanical testing, and x-ray computed tomography were utilized to analyze microstructure, mechanical performance, and surface roughness. With an increase in particle size of the HH, the corresponding biocomposites showed increased flowability, and the injection-molded specimens showed increased impact strength. The FFF printing of the biocomposite filament presented no challenges, and the mechanical properties of FFF parts enhanced with a particle size smaller than the printed layer thickness. Compared with injection-molded parts, FFF-printed samples showed higher impact strength. The FFF-printed PLA/HH biocomposite samples showed considerable potential over their injection molded alternatives for low-volume specialized applications.

Highlights

- Polylactide (PLA)/hemp hurd (HH) biocomposite filaments with different particle sizes of HH were developed.
- Melt flow and impact strength increased when HH particle size increased.
- 3D-printed part porosity and roughness increased when HH particle size increased.
- Higher HH particle size enhanced the mechanical performance of 3D-printed parts.
- 3D-printed parts exhibited higher impact strength than injection molded parts

This is an open access article under the terms of the [Creative Commons Attribution-NonCommercial](https://creativecommons.org/licenses/by-nc/4.0/) License, which permits use, distribution and reproduction in any medium, provided the original work is properly cited and is not used for commercial purposes.

© 2024 The Author(s). *Polymer Composites* published by Wiley Periodicals LLC on behalf of Society of Plastics Engineers.

KEYWORDS

3D printing, hemp hurd, mechanical properties, particle size, polylactic acid, porosity, surface roughness

1 | INTRODUCTION

Poly lactide (PLA) biopolymer is widely used in 3D printing,^{1–3} furnishings, building and construction,⁴ automobiles, and packaging applications because of its superior mechanical properties,^{1,2} dimensional stability, biocompatibility, and biodegradability.^{5–10} PLA although exhibits shortcomings in cost effectiveness, crystallization during processing¹¹ and moderate toxicity during 3D printing, albeit lower than the common 3D printing synthetic polymers such as acrylonitrile butadiene styrene (ABS).¹² To this end, biomass use in PLA-based biocomposites has attracted increasing attention as feedstock for fused filament fabrication (FFF) applications, as they offset the baseline polymer fraction and accelerate their end-of-life degradation.¹³ Biocomposite feedstock for FFF is mainly processed using melt-compounding of PLA with continuous fibers,¹⁴ and biomass such as bamboo,¹⁵ lignin,^{16,17} cork,¹⁸ flax fiber,¹⁹ and wood flour,¹² ramie fiber,²⁰ and hemp hurd (HH).^{1,21}

Industrial HH is a key biomass source derived from hemp fiber production and often disposed of by combustion or landfilling, causing resource loss and environmental pollution. The utilization of HH in PLA biocomposite leads to valorization, and often considered as a strong substitute for wood-based fillers because of its higher cellulose fraction.²² PLA/HH biocomposite was developed for antibacterial packaging by Khan et al. who also investigated the efficacy of HH in glycidyl methacrylate-grafted PLA (GMA-g-PLA).^{17,18} GMA-g-PLA effectively enhanced the compatibility of PLA/HH biocomposites, with the biocomposite with a 20 wt% HH inclusion in GMA-g-PLA exhibiting the optimum thermal/mechanical properties. In a recent work by the authors, FFF-printed components with incorporation of increasing content of HH in PLA biocomposites feedstock were systematically investigated, the authors found that up to 30 phr content of HH in PLA exhibited near equivalent impact strength compared to commercial PLA FFF feedstock, while the surface roughness increased and tensile strength decreased discernibly for 3D printed parts when HH content increased from 20 to 30 phr.¹

The higher surface roughness and porosity, and decreased mechanical strength are resultant of an increasing biomass fraction in FFF PLA biocomposite feedstock,^{1,23–25} also controlled by the parameters of 3D printing, including printing temperature, printing speed, layer height,^{26–28}

printing orientation, and air gap although in contrast, surface roughness is predominantly is dictated by printed layer height (thickness).^{29–31} At constant biomass weight fraction and printing parameters, it could be conjectured based on published data^{32,33} that the biomass, for example, HH particle aspect ratio (length/diameter) drives the (i) surface quality and (ii) mechanical properties. Zhao et al.³⁴ investigated the effect of poplar fiber size on the thermo-mechanical and rheological properties of PLA biocomposites and assessed their suitability for large-scale 3D printing, and reported that poplar fiber particle size less than 180 μm was favorable for obtaining optimal processing viscosity range and tensile strength for PLA/poplar biocomposites, but the research did not investigate the biomass particle size effect on the performance of 3D printed parts. A comparable study³⁵ reported that a decreasing particle size resulted in increase in both tensile strength and Young's modulus, whereas slightly causing a decrease in the toughness (elongation-at-break) for PLA/paulownia wood powder biocomposites. 3D printing with biomass biocomposites could be challenging, which is attributed to potential nozzle clogging, relatively rougher surface and higher porosity than neat PLA. These challenges are closely related to the biomass particle size.^{1,9,14,23} Yiga et al.³⁶ reported the inclusion of rice husk decreased the tensile strength whereas increased the tensile modulus of PLA/clay/rice husk composites. Rodvalho et al.³⁷ investigated nanohydroxyapatite (nHA) size influence on the 3D printed scaffolds made from PLA/nHA, and found that the smallest particle size was beneficial for improving the compressive strength. To date, no comprehensive investigations regarding the HH particle size influence on PLA based biocomposite FFF feedstock for 3D printing application have been conducted.

Systematic research on the correlation between particle size of HH and the rheological behavior, morphology, mechanical performance, and surface characteristics that is, engineering the surface finish of PLA-based biocomposites feedstock is beneficial towards the application potential of HH and by extension, comparable biomass fillers in FFF applications. A relatively unexplored aspect of the research of PLA biocomposites for FFF applications is the influence of biomass particle size on overall performance. This work aimed to study how HH particle size influences rheological behavior, microstructure, and mechanical performance of PLA/HH feedstock and parts prepared by injection and FFF. In this work, PLA/HH

biocomposite filaments using untreated HH with variable particle sizes have been developed as economical feedstock for FFF applications. Untreated HH was melt-blended followed by extrusion with PLA and a toughening agent poly(butylene adipate-co-terephthalate) (PBAT), and compatibilized using ethylene-methyl acrylate-glycidyl methacrylate terpolymer (EGMA) through a rotational twin-screw extruder and pelletized and processed as a FFF filament utilizing a single-screw extruder. The rheological, mechanical performances, surface morphology, and porosity of PLA/HH feedstock were investigated on FFF-printed parts and compared with comparable traditional injection-molded (IM) components. FFF-printed samples were assessed via the analysis of printability, surface quality, and microstructure to explain the key underlying mechanisms to gain valuable insights for future design and engineering of furnishings, building and construction, automobiles, and packaging applications.

2 | MATERIALS AND METHODS

2.1 | Materials

Commercial grade PLA 4032D was supplied by NatureWorks LLC. PBAT 2003F with a melt flow rate of 4.2 g/10 min (at 190°C, 2.16 kg) was purchased from Zhejiang Hangzhou Xinfu Pharm Co., Ltd. EGMA AX 8900, was procured from Arkema, Inc. PLA and PBAT pellets were dried in a conventional oven before use to achieve a moisture content <0.3 wt%. HH (Yunnan Dama Co., Ltd) was supplied in the form of chips, which were milled using a jet grinder and sorted through vibrating screens of 100, 200 and 300 mesh sizes. The obtained HH powder was labeled as HH-1 (passing 300 mesh), HH-2 (intermediate to 200–300 mesh), and HH-3 (intermediate to 100–200 mesh), respectively. HH powder was dried out to a moisture content <0.5 wt% prior to processing. An anti-hydrolysis agent, Carbodiimide HMV-15CA was obtained from Nissinbo Chemicals, Inc., and antioxidants 1010 and 168, and ethylene bis stearamide lubricant additives were introduced to improve the stability and processability of the compounds and used as received.

2.2 | Biocomposite feedstock and FFF filament processing

PLA/HH biocomposite processing involved the melt-blending of PLA/PBAT/EGMA with HH of various particle sizes, as formulations shown in Table 1. The processed biocomposites, i.e., PLA-HH-1, PLA-HH-2, and PLA-HH-3 correspond to the addition of HH-1, HH-2,

TABLE 1 Constituent of the developed polylactide/hemp hurd (PLA/HH) biocomposites filled with HH possessing various particle size.

Constituent	PLA	PBAT	HH	EGMA	Additives
Concentration (phr)	87	13	20	6.5	2.2

and HH-3, respectively. A formulation without HH was also processed and labeled as PLA-HH-0. These biocomposites were extruded using a parallel twin-screw extruder (D = 35 mm, L/D = 44) at a temperature profile extending from 165 to 175°C, and pelletized. The feeder temperature was set to 110°C to avoid the melting of PLA and PBAT, and to preclude clogging in the extruder barrel. The as-obtained pellets were then processed as filaments using extrusion conducted on a single-screw extruder (D = 35 mm, L/D = 28). The extrusion temperatures were set at 170–180°C, with a 364 rpm screw speed. The filament with a 1.75 mm design diameter was drawn at 351 rpm spool speed after immersing in 60°C-water-bath for cooling and was collected on spools.

2.3 | Specimen Preparation

Both FFF-printed and Injection molded (IM) samples were produced in this study. Specimens for tensile test (166 mm × 19 mm × 3.2 mm, Type I, ASTM D638), and notched impact test (63 mm × 12.7 mm × 3.2 mm, ASTM D256) were injection-molded on an injection molding machine (JT-350, Jintong Plastic Machinery Ltd., China). The temperatures of barrel zones were set to 165, 175, 175, and 182°C, the mold temperature was 45°C.

Similar standard testing specimens were printed using a 3D printer (da Vinci 1.0 professional, XYZ Printing, Inc.) in a flat orientation, with a nozzle of 0.4 mm diameter. The printing conditions used were 200°C in nozzle temperature, 60°C in print bed temperature, 100% in infill density, 0.15 mm in layer height, and 60 mm/s in printing speed.

2.4 | Characterization and testing

HH powder morphology and IM specimen fracture surface were analyzed on a Hitachi SU3500 SEM after coating with a gold layer, at 15 keV. FFF-printed specimen impact fracture surface was evaluated using JEOL JCM6000 SEM (5–15 keV). The fracture surface of the FFF filament was imaged on a JEOL JSM 7100F SEM (2 keV), on a cross-section cut using a razor blade and coated with 15-nm Pt using a Quorum Q150T metal coater.

Particle size analysis including distribution for HH powder was conducted on a Mastersizer 2000 dynamic laser

particle size analyzer (Malvern Instruments Ltd.) in the 0.02–2000 μm size range resolution, using water as the dispersant with a refractive index = 1.34. The 50% intercept of the cumulative volume that is, d_{50} was calculated using vendor software denoting the particle size at 50% undersize.

Rheology testing was performed using a DHR-2 rotational rheometer (TA Instruments, USA), outfitted with a parallel plate of diameter = 25 mm and gap = 1 mm. Dynamic frequency sweep mode from 0.0628 rad/s to 628 rad/s at 190°C with a strain amplitude of 1% was used for the tests. Melt flow rate (MFR) testing was conducted on a melt flow indexing device (XNR-400C, Taian Ontime Testing Machine Manufacturing Co., Ltd) at 190°C, 2.16 kg (ASTM D1238 Condition E).

Tensile testing was conducted on a universal testing machine (CMT 6104, MTS Systems, China) using a 10 kN load cell, following ASTM D 638, at a crosshead displacement rate of 5 mm/min. Notched Izod impact testing was conducted to determine impact strength on XJJU 5.5J pendulum from Chengde COTs Scientific Instruments Co., Ltd. at room conditions following ASTM D 256. At least five specimens for each sample were examined, and the average values have been reported.

The surface roughness of FFF-printed specimens were determined using a MarSurf M 400 instrument (stylus tip diameter = 2 μm , tip angle = 90°, tracing

speed = 1.0 mm/s, trace length = 17.50 mm). Roughness parameters including arithmetic mean roughness (R_a), root mean square roughness (R_q), mean peak-to-valley height (R_z), and maximum peak-to-valley height (R_{max}) were calculated following the ISO 4287 standard.

The porosity fields of the FFF specimens were scanned by x-ray computed tomography (XCT) on an instrument (General Electric Phoenix v|tome|x) operating at the micro-level, scanned at 50 kV and 90 μA (voxel size = 8.0 μm). The two-dimensional sectional images were extracted and utilized to confirm microstructural characteristics in the specimens. A three-dimensional volumetric representation of the specimens was created using the obtained image projections. The XCT scan information converted to microstructure and the porosity data in the FFF specimens was determined using the Porosity/Inclusion Analysis Module in the VolMaxStudio 3.0 Program.

3 | RESULTS AND DISCUSSION

3.1 | Morphology and particle size distribution of HH powder

The morphological analysis involved the acquisition of SEM images (Figure 1A–C) and particle size distribution

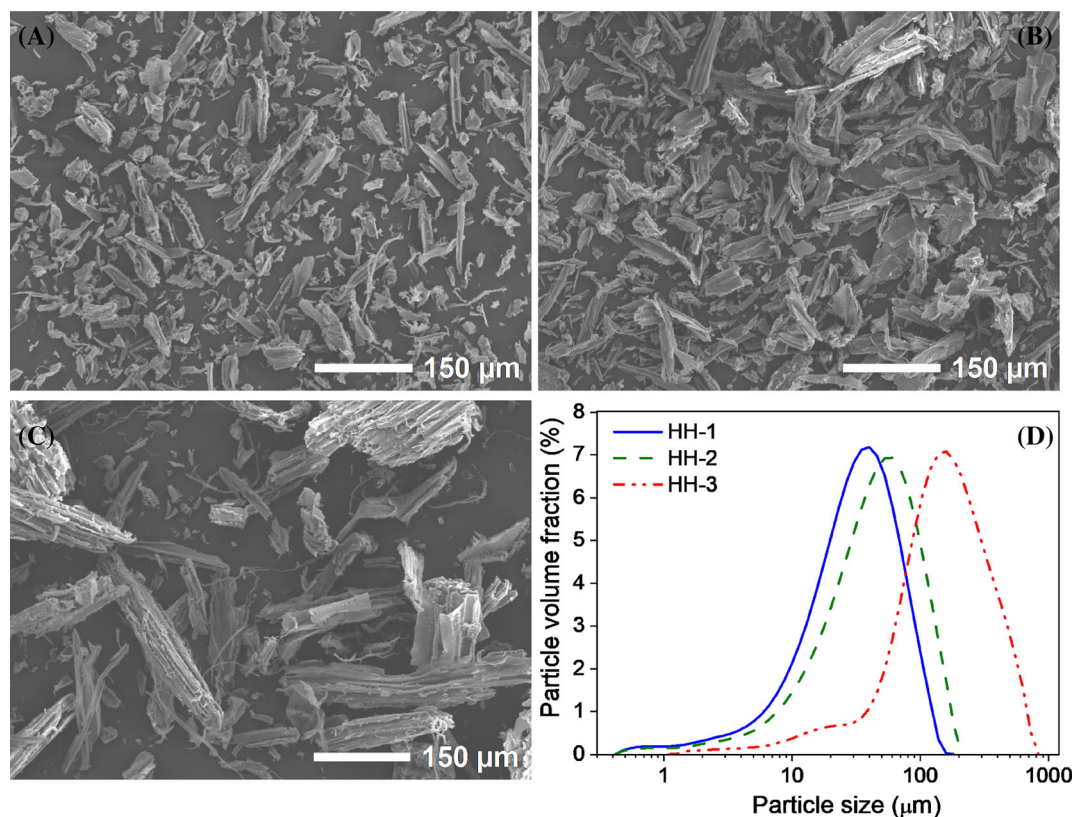


FIGURE 1 Morphology of the HH powders as imaged using SEM, showing (A) HH-1, (B) HH-2, and (C) HH-3 at 150 \times magnification and (D) their particle size distribution.

(Figure 1D) of HH powder. Figure 1A–C elucidate the micro-morphology of HH-1, HH-2, and HH-3, respectively. The SEM images illustrate a fibrillated HH structure with an increasing aspect ratio (l/d) from HH-1 to HH-3 as the particle size increased, which supported the values of HH particle size distribution in Figure 1D. The elongated shape ($l \gg d$) of the HH particles as discernible from the SEM images, permitted to pass through lower-numbered (or larger particle size) meshes during sieving. The volume-median-diameter (d_{50}) of HH-1, HH-2, and HH-3 were 35, 50, and 160 μm , respectively.

3.2 | Specimen properties of PLA/HH biocomposites

3.2.1 | Rheology and melt flowability

Rheological behavior during melt state was measured to assess processability and internal structure of PLA/HH

biocomposites, as seen in the rheometry data provided in Figure 2. The slope of $\log G'$ versus $\log G''$ plot was used to determine if the constituents are miscible/compatible. For miscible systems, the slope of $\log G'$ versus $\log G''$ is similar to the base polymer matrix.³⁸ In this study, PLA/HH biocomposites showed a lower slope on $\log G'$ versus $\log G''$ plot than the unfilled polymer matrix (PLA-HH-0), as shown in Figure 2A, indicating HH and PLA are only partially miscible. PLA-HH-1 showed higher G' , G'' , and $|\eta^*|$ values in comparison to the other biocomposites at a frequency lower than 3 rad/s (Figure 2B,C). With increasing HH particle size, G' and $|\eta^*|$ decreased, consistent with the MFR data from tests at Condition E (Figure 2D), and as reported by Hristov et al.,³⁹ supporting smaller particles offer higher resistance to deformation, whereas the larger particles are prone to flow because of the increased wetting caused by their lower specific surface area.⁴⁰ The smaller particles also facilitate formation of networks within the polymer matrix.⁴¹ The rheological properties were overall similar

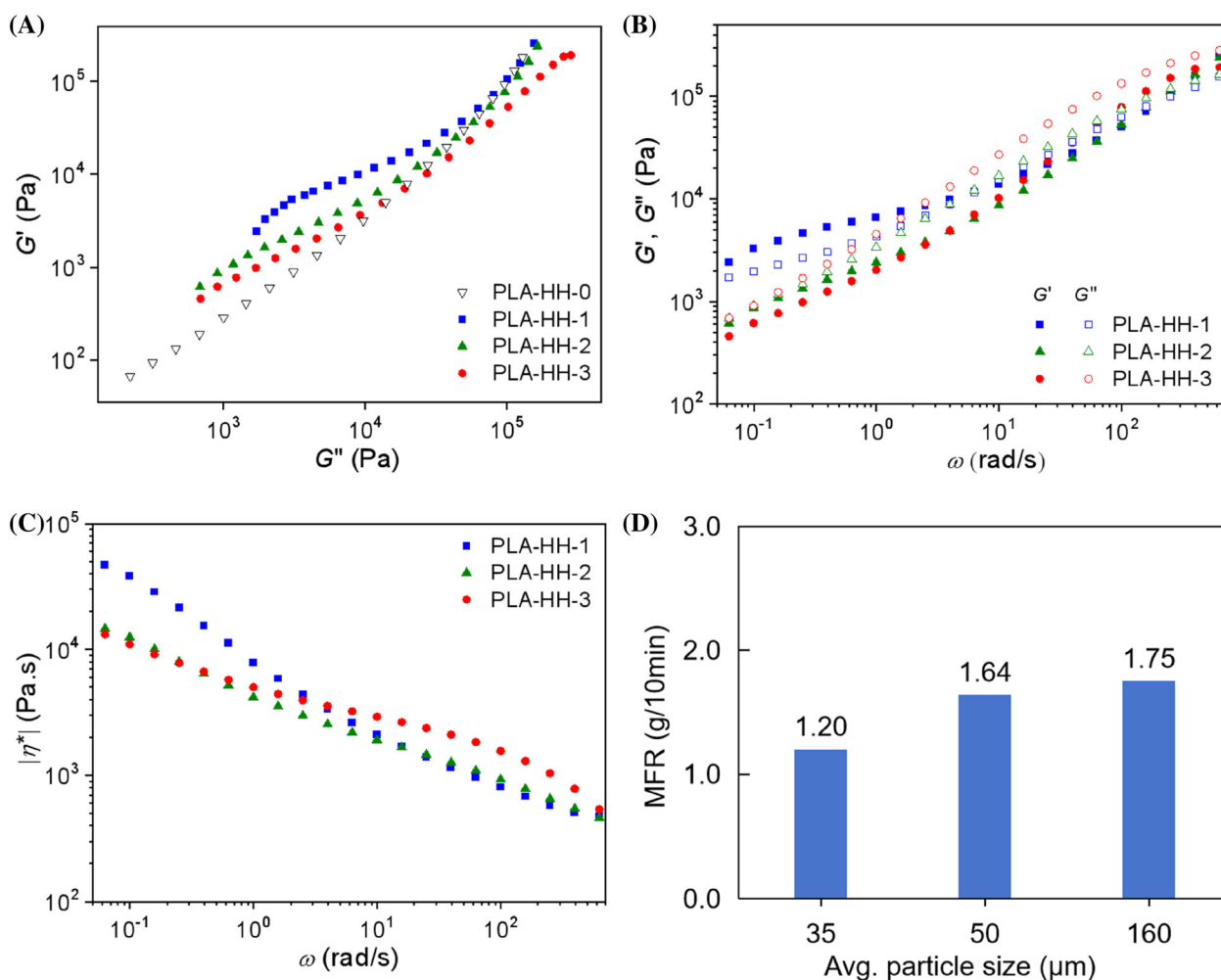


FIGURE 2 Rheology analysis of poly(lactide)/hemp hurd biocomposite feedstock showing: (A) $\log G'$ - $\log G''$, (B) G' , G'' , (C) $|\eta^*|$, and (D) melt flow rate data.

at high dynamic frequency because of the possible disentanglement of polymer chains and the decreased particle-particle interactions. PLA-HH-1 exhibited elastic behavior ($G' > G''$) at a frequency below 10 rad/s, however PLA-HH-2 and PLA-HH-3 demonstrated viscous behavior ($G'' > G'$) over the whole frequency range (Figure 2B). Both rheological behavior and MFR data demonstrated that incorporation of smaller particle size HH resulted in a lowered melt flow for the processed PLA/HH biocomposites.

3.2.2 | Dispersion of HH and interface morphologies

SEM imaging was acquired to explain the particle size effects on HH dispersion in the PLA matrix, and to investigate the cryo-fractured surface morphology of IM specimens, as shown in the SEM micrographs in Figure 3. HH dispersed in the polymer matrix parallelly mostly and maintained its original fibrillated structure. In PLA-HH-1 (Figure 3A), HH debonding from the polymer matrix was detected throughout the fracture surface, suggesting an insufficient interfacial adhesion at HH/PLA interface. The extent of HH/polymer matrix adhesion in PLA-HH-2 was demonstrable with HH retaining a greater l/d over PLA-HH-1, attributed to the elongated HH2 particles. Failure in PLA-HH-3 was constricted within the HH fiber, rather than pull-out or debonding at the interface, which affirmed that effective interfacial adhesion was achieved, along with potentially efficient filler-to-matrix transfer of applied stress.

3.2.3 | Mechanical properties

HH particle size effect was correlated with the mechanical properties of IM specimens prepared from the PLA/HH biocomposites (PLA-HH-1–PLA-HH-3), and

the results are summarized in Table 2. PLA/HH specimens exhibited similar tensile strength (~ 50 MPa), except PLA-HH-1, which showed a lower tensile strength of 47.2 MPa. This variation in the tensile strength at constant weight fraction is driven by interfacial compatibility and interfacial area, which in turn dictate stress transfer and failure. Because of the inadequate interfacial adhesion confirmed by the morphological analysis of the interface and the high interfacial area confirmed through particle analysis, PLA-HH-1 showed slightly inferior response to tensile stress, readily yielding under load,⁴² as further evidenced by prevalent HH pull-out (Figure 3A) at the interface. The elongation-at-break marginally decreased with a corresponding increase in HH particle size. The impact strength increased with an increase in HH particle size, as expected. PLA-HH-1 displayed an impact strength = 41.3 J/m, which was lower compared to PLA-HH-3 (54.4 J/m) because of the superior filler-matrix stress transfer. This result is consistent with the literature report on PVC/rice hull biocomposites,⁴³ and in this study, supported by the SEM analysis (Figure 3C).

3.3 | Morphology of FFF filament

Cross-sectional surfaces of PLA/HH filaments were analyzed using SEM, and the micrographs are shown in Figure 4. From Figure 4A–C, PLA/HH filament cross

TABLE 2 Mechanical properties of injection-molded specimens as a function of hemp hurd (HH) particle size.

Materials	Tensile strength (MPa)	Elongation at break (%)	Impact strength (J/m)
PLA-HH-1	47.2 ± 0.9	13.9 ± 1.18	41.3 ± 3.0
PLA-HH-2	50.8 ± 1.8	13.2 ± 1.29	46.4 ± 1.6
PLA-HH-3	50.3 ± 0.3	12.7 ± 1.20	54.4 ± 4.3

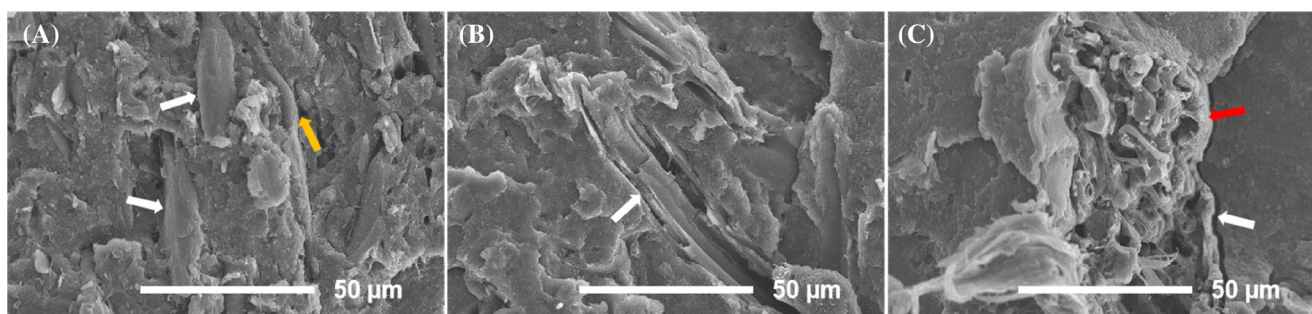
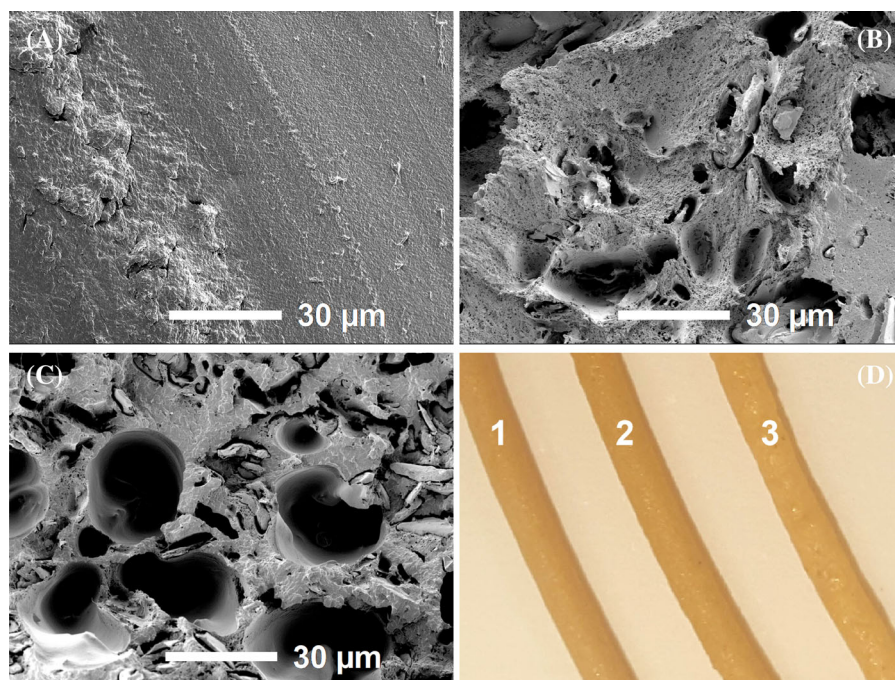


FIGURE 3 SEM images of the cryo-fractured surface morphology of injection-molded PLA/HH samples: (A) polylactide-hemp hurd (PLA-HH)-1, (B) PLA-HH-2, and (C) PLA-HH-3.

FIGURE 4 SEM images of the razor-cut cross section of the PLA/HH filaments: (A) PLA-HH-1, (B) PLA-HH-2, and (C) PLA-HH-3, (D) PLA/HH filaments produced from (1) PLA-HH-1, (2) PLA-HH-2, and (3) PLA-HH-3.



section showed increased porosity as HH particle size increased, with pore size also increased from Figure 4A–C, attributed to the increased HH particle size. One parameter that could affect the increase in filament porosity could be the decreased viscosity, which led to the decreased melt pressure in the extruder barrel during filament extrusion and caused the looser internal structure of filaments. The manufactured PLA/HH filaments exhibited increasing surface roughness with HH particle size increases as illustrated in Figure 4D.

3.4 | Properties of FFF-printed specimens

3.4.1 | Surface roughness

Surface roughness analysis of PLA/HH filaments involved correlation with HH particle size as presented in Figure 5. Overall, average roughness (R_a) values were $\sim 20 \mu\text{m}$. The roughness of PLA-HH-1 and PLA-HH-2 were near similar because the constituent HH particle size was of a lower dimension than the height of the printing layer ($150 \mu\text{m}$). The roughness of PLA-HH-3 was marginally higher than the other biocomposite filaments because of HH particle size $>150 \mu\text{m}$, which was the height of the printing layer. The FFF printing of PLA-HH-3 revealed nozzle jamming and clogging, despite high MFR of the biocomposites, causing disruption in FFF part fabrication. These processing challenges are resultant of larger HH particles impeding melt flow

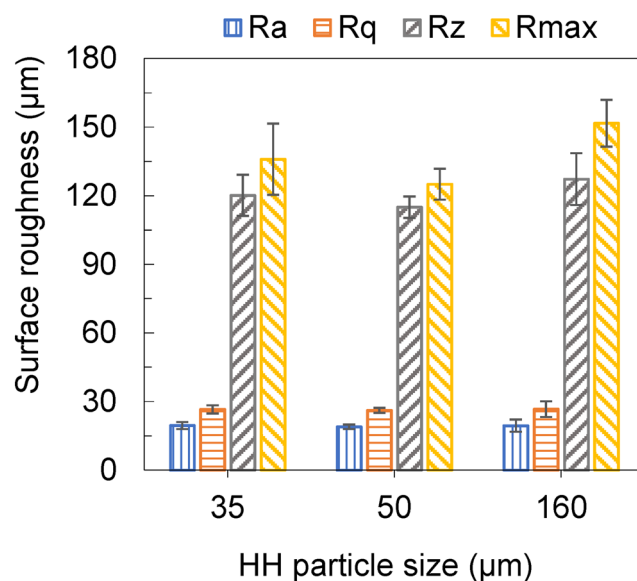


FIGURE 5 The surface roughness trend of FFF-printed specimens correlated to the variation in HH particle size.

throughput at the nozzle, which results also in the enhanced surface roughness of the filament and eventually, FFF-printed parts.

3.4.2 | Porosity

Porosity in FFF-printed sample was characterized by XCT to correlate HH particle size with the interfacial

adhesion between adjacent layers. Cross-sectional image slices acquired parallel to the printing direction of the specimens, as shown in Figure 6. The size distribution of the voids is denoted through an assortment of colors. With an increase in HH particle size, XCT analysis elucidated an increase in volume fraction of porosity and increase in average pore size along the direction of printing (purple arrows in Figure 6D). The porosity of PLA/HH specimens gradually increased in the samples that is, PLA-HH-1, PLA-HH-2, and PLA-HH-3 showing 4.86%, 6.34%, and 9.85% volume fractions, respectively. An overall increase in porosity and pore size is driven by insufficient interlayer fusion bonding, which in turn decreases because HH particle size increases. The voids were located between layers, as highlighted with black solid rectangles in Figure 6E,F, due to the insufficient fusion between adjacent layers. The distribution of voids along the FFF print tracks suggested the lack of melt fusion in representative areas lying between adjacent tracks, and because of the confinement of volatiles within voids.⁴⁴ Overall, XCT analysis revealed a critical correlation between the variation in particle size, and interlayer melt fusion and bonding.

3.4.3 | Morphology

Impact fracture in FFF specimens was analyzed using SEM, as shown in Figure 7. The fracture surfaces became discernibly and gradually rougher with an increase in HH particle size. Increased porosity and larger interlayer space were realized concomitantly, further confirming the XCT imaging (Figure 6). All

specimens exhibited elastoplastic deformation, with fibrillated, long superficial fragments, which led to enhanced impact strength compared with IM samples (See Table 2). PLA-HH-3 displayed a smoother fracture surface compared to PLA-HH-1 and PLA-HH-2, with large surface voids, leading to slight increase in impact strength against IM samples, as shown in Table 2.

3.4.4 | Mechanical properties

Analysis of mechanical properties focusing on toughness is critical for achieving optimal printability, and application development with the feedstock. The mechanical properties of FFF-printed samples are shown in Table 3. All the specimens exhibited higher impact strength than commercial PLA printed samples.¹ Mechanical performance including the data on tensile strength, elongation-at-break and impact strength values showed an increase with corresponding increase in HH particle size from 35 to 50 μm , which in turn dictated the increased interfacial adhesion between HH and PLA matrix. Whereas all the mechanical performances decreased with a HH particle size $>160 \mu\text{m}$, because of the significant increase in porosity and pore sizes. All FFF-printed samples showed higher levels of impact strength compared to their IM equivalents (Table 1), which is consistent with the results obtained from our previous work,¹ where we found that FFF-printed specimens overall exhibited higher impact strength than their injection molded counterparts.

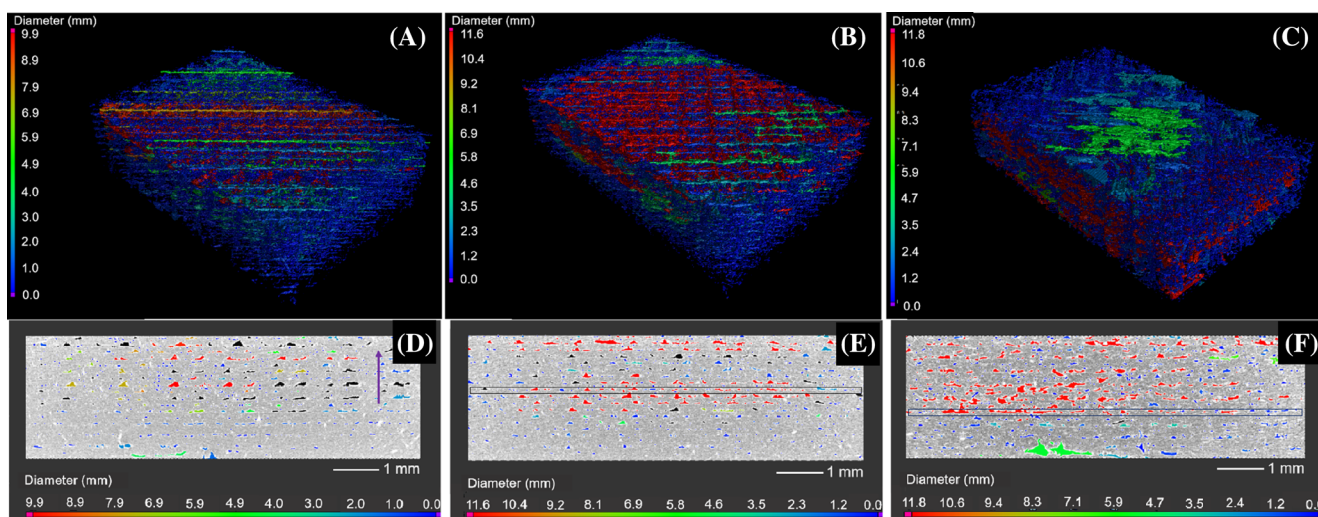


FIGURE 6 3D porosity distribution as elucidated via XCT image slices (top view) of FFF-printed specimens: (A,D) polylactide-hemp hurd (PLA-HH)-1, (B,E) PLA-HH-2, and (C,F) PLA-HH-3.

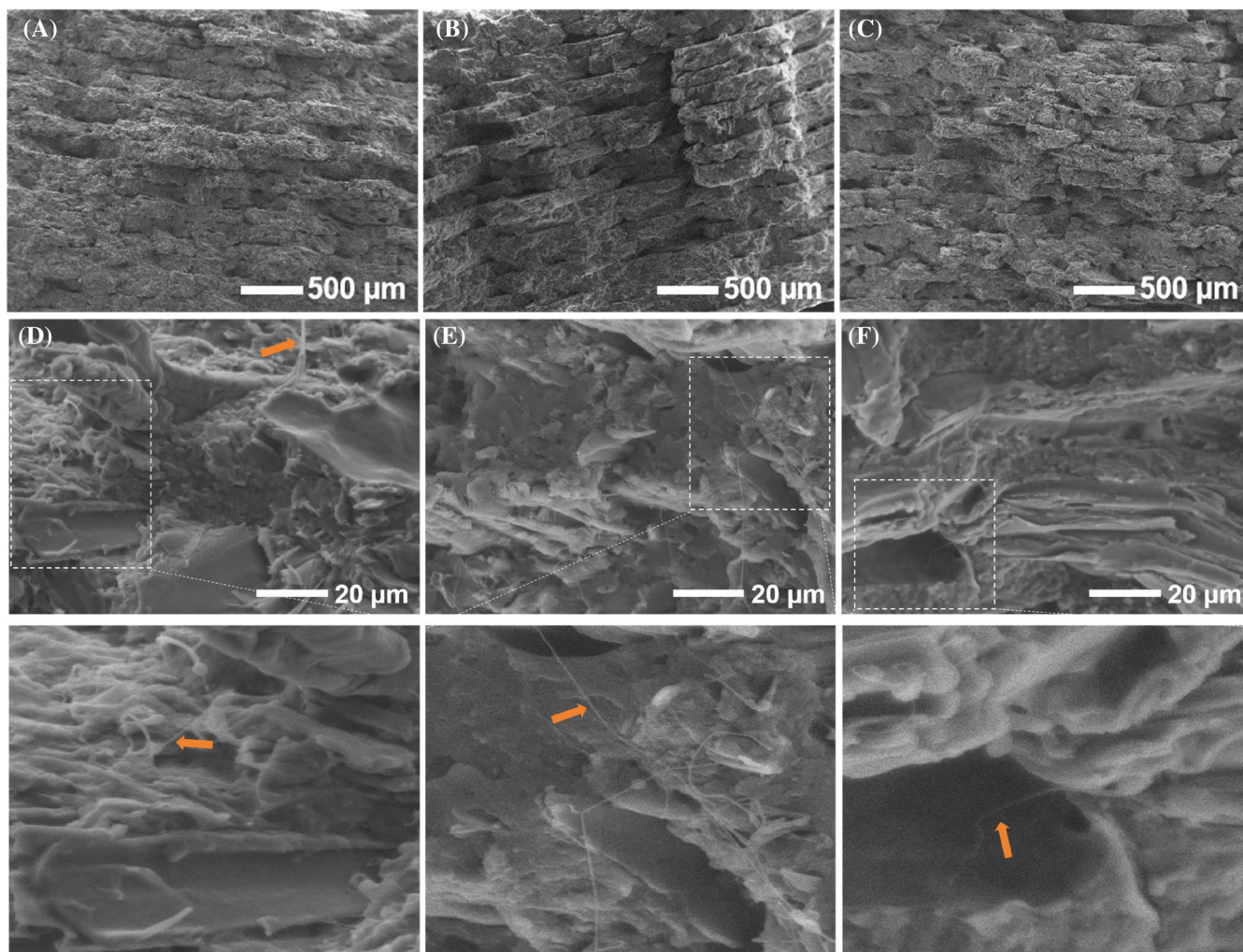


FIGURE 7 SEM imagery of the impact fracture surface in FFF samples: (A, D)PLA-HH-1, (B, E) PLA-HH-2, and (C, F) PLA-HH-3.

TABLE 3 Mechanical properties of fused filament fabrication-printed specimens as a function of hemp hurd (HH) particle size.

Materials	Tensile strength (MPa)	Elongation at break (%)	Impact strength (J/m)
PLA-HH-1	30.5 ± 0.9	6.96 ± 0.16	55.1 ± 2.0
PLA-HH-2	33.9 ± 2.1	9.74 ± 0.20	56.6 ± 5.4
PLA-HH-3	29.6 ± 0.7	8.22 ± 0.26	55.5 ± 2.2

4 | CONCLUSIONS

This systematic investigation of the rheological behavior, printability, microstructure, mechanical properties, and surface quality of PLA/HH biocomposite as FFF feedstock focused on the effects of HH particle size variation. An increased HH particle size led to higher melt flowability and increased impact strength for IM specimens. The

FFF-printed specimens exhibited similar surface roughness and improved mechanical properties with increase HH particle size when the particle sizes were 35 and 50 μm , which are lower than the layer height of 150 μm . The filament presented challenge in FFF printing when HH particle size reached 160 μm , which is higher than print layer height. In general, higher impact strength was realized in FFF samples over IM samples. Overall, bigger particle size under the print layer height is favorable for achieving optimal properties for FFF parts. This investigation established the connections between the particle size of HH and a range of key material properties of FFF PLA/HH biocomposite feedstock.

ACKNOWLEDGMENTS

The authors acknowledge Dr. Philippa Uwins, Dr. Lakshmi Srinivasamurthy, Dr. Zhanhui Zhang, Dr. Jianying Wang, Dr. Tonghui Hao, and Dr. Dongning He for their technical assistance. Open access publishing

facilitated by University of Southern Queensland, as part of the Wiley - University of Southern Queensland agreement via the Council of Australian University Librarians.

FUNDING INFORMATION

This work was supported by the Forest and Wood Products Australia (Grant number PNA360-1516), Australian Research Council projects DP230103008 and IH220100002, College Student Innovation and Entrepreneurship Training Program Grant No. S202411528190, and the Scientific Research Fund of Hunan Provincial Education Department (Grant number 21A0569 and 21A0569).

DATA AVAILABILITY STATEMENT

The data that support the findings of this study are available from the corresponding author upon reasonable request.

ORCID

Xianglian Xiao  <https://orcid.org/0000-0002-4622-3467>
Venkata S. Chevali  <https://orcid.org/0000-0002-5648-0344>

REFERENCES

- Xiao X, Chevali VS, Song P, He D, Wang H. Polylactide/hemp hurd biocomposites as sustainable 3D printing feedstock. *Compos Sci Technol*. 2019;184:107887. doi:10.1016/j.compscitech.2019.107887
- Xiao X, Chevali VS, Song P, Yu B, Yang Y, Wang H. Enhanced toughness of PLLA/PCL blends using poly(D-lactide)-poly(L-caprolactone)-poly(D-lactide) as compatibilizer. *Compos Commun*. 2020;21:100385. doi:10.1016/j.coco.2020.100385
- Dananjaya SAV, Chevali VS, Dear JP, Potluri P, Abeykoon C. 3D printing of biodegradable polymers and their composites—current state-of-the-art, properties, applications, and machine learning for potential future applications. *Prog Mater Sci*. 2024;146:101336. doi:10.1016/j.pmatsci.2024.101336
- Zhang Y, Liu L, Yao M, et al. Functionalizing lignin by in situ solid-phase grafting ammonium polyphosphate for enhancing thermal, flame-retardant, mechanical, and UV-resistant properties of polylactic acid. *Chem Eng J*. 2024;495:153429. doi:10.1016/j.cej.2024.153429
- Khan BA. *Development of Antibacterial Hemp Hurd/Poly(Lactic Acid) Biocomposite for Food Packaging*. University of Southern Queensland, Australia 2017.
- Khan BA, Warner P, Wang H. Antibacterial properties of hemp and other natural fibre plants: a review. *Bioresources*. 2014;9(2):3642-3659.
- Chevali VS, Srinivasamurthy L, Khan B, Wang H. Experimental and molecular dynamics analysis of antimicrobial additive migration from biocomposite packaging. *Proceedings of the 22nd International Conference on Composite Materials (ICCM-22)*. Engineers Australia; 2019. doi:10.3316/informit.862320981209163
- Khan BA, Wang J, Warner P, Wang H. Antibacterial properties of hemp hurd powder against *E. coli*. *J Appl Polym Sci*. 2015;132(10):41588.
- Khan BA, Na H, Chevali V, Warner P, Zhu J, Wang H. Glycidyl methacrylate-compatible poly(lactic acid)/hemp hurd biocomposites: processing, crystallization, and thermo-mechanical response. *J Mater Sci Technol*. 2018;34(2):387-397. doi:10.1016/j.jmst.2017.03.004
- Khan BA, Chevali VS, Na H, Zhu J, Warner P, Wang H. Processing and properties of antibacterial silver nanoparticle-loaded hemp hurd/poly(lactic acid) biocomposites. *Compos Part B: Eng*. 2016;100:10-18. doi:10.1016/j.compositesb.2016.06.022
- Tawiah B, Yu B, Wei R, et al. Simultaneous fire safety enhancement and mechanical reinforcement of poly(lactic acid) biocomposites with hexaphenyl (nitro)tris(ethane-2,1-diyl)tris(phosphoramidate). *J Hazard Mater*. 2019;380:380. doi:10.1016/j.jhazmat.2019.120856
- Zhang Q, Pardo M, Rudich Y, et al. Chemical composition and toxicity of particles emitted from a consumer-level 3D printer using various materials. *Environ Sci Technol*. 2019;53(20):12054-12061. doi:10.1021/acs.est.9b04168
- Momeni S, Craplewe K, Safder M, Luz S, Sauvageau D, Elias A. Accelerating the biodegradation of poly(lactic acid) through the inclusion of plant fibers: a review of recent advances. *ACS Sustain Chem Eng*. 2023;11(42):15146-15170. doi:10.1021/acssuschemeng.3c04240
- Tao Y, Li P, Zhang J, Wang S, Shi SQ, Kong F. A review of fused filament fabrication of continuous natural fiber reinforced thermoplastic composites: techniques and materials. *Polym Compos*. 2023;44(12):8200-8222. doi:10.1002/pc.27477
- Xiao X, Chevali VS, Wang H. Toughening of polylactide/bamboo powder biocomposite for 3D printing. *Proceedings of the 22nd International Conference on Composite Materials (ICCM-22)*. Engineers Australia; 2019. doi:10.3316/informit.874003854188054
- Ding R, Duan Z, Sun Y, et al. Enhancement of 3D printability and mechanical properties of polylactic acid/lignin biocomposites via interface engineering. *Ind Crop Prod*. 2023;194:194. doi:10.1016/j.indcrop.2023.116286
- Johansson M, Skrifvars M, Kadi N, Dhakal HN. Effect of lignin acetylation on the mechanical properties of lignin-poly-lactic acid biocomposites for advanced applications. *Ind Crop Prod*. 2023;202:202. doi:10.1016/j.indcrop.2023.117049
- Daver F, Lee KPM, Brandt M, Shanks R. Cork-PLA composite filaments for fused deposition modelling. *Compos Sci Technol*. 2018;168:230-237. doi:10.1016/j.compscitech.2018.10.008
- Le Duigou A, Barbé A, Guillou E, Castro M. 3D printing of continuous flax fibre reinforced biocomposites for structural applications. *Mater Des*. 2019;180:180. doi:10.1016/j.matdes.2019.107884
- Cheng P, Wang K, Chen X, et al. Interfacial and mechanical properties of continuous ramie fiber reinforced biocomposites fabricated by in-situ impregnated 3D printing. *Ind Crop Prod*. 2021;170:170. doi:10.1016/j.indcrop.2021.113760
- Jubenville D, Sharifi J, Fayazfar H, Mekonnen TH. Hemp hurd filled PLA-PBAT blend biocomposites compatible with additive manufacturing processes: fabrication, rheology, and material property investigations. *Polym Compos*. 2023;44(12):8946-8961. doi:10.1002/pc.27749
- Li X, Xiao R, Morrell JJ, Zhou X, Du G. Improving the performance of hemp hurd/polypropylene composites using pectinase pre-treatments. *Ind Crop Prod*. 2017;97:465-468. doi:10.1016/j.indcrop.2016.12.061

23. Kariz M, Sernek M, Obućina M, Kuzman MK. Effect of wood content in FDM filament on properties of 3D printed parts. *Mater Today Commun.* 2018;14:135-140. doi:10.1016/j.mtcomm.2017.12.016
24. Ayrlmis N, Kariž M, Kitek Kuzman M. Effect of wood flour content on surface properties of 3D printed materials produced from wood flour/PLA filament. *Int J Polym Anal Charact.* 2019;24(7):659-666. doi:10.1080/1023666X.2019.1651547
25. Tao Y, Kong F, Li Z, et al. A review on voids of 3D printed parts by fused filament fabrication. *J Mater Res Technol.* 2021;15:4860-4879. doi:10.1016/j.jmrt.2021.10.108
26. Ayrlmis N. Effect of layer thickness on surface properties of 3D printed materials produced from wood flour/PLA filament. *Polym Test.* 2018;71:163-166. doi:10.1016/j.polymertesting.2018.09.009
27. Hartcher-O'Brien J, Evers J, Tempelman E. Surface roughness of 3D printed materials: comparing physical measurements and human perception. *Mater Today Commun.* 2019;19:300-305. doi:10.1016/j.mtcomm.2019.01.008
28. Kang B, Hyeon J, So H. Facile microfabrication of 3-dimensional (3D) hydrophobic polymer surfaces using 3D printing technology. *Appl Surf Sci.* 2020;499:499. doi:10.1016/j.apsusc.2019.143733
29. Vidakis N, David C, Petousis M, Sagris D, Mountakis N, Moutsopoulou A. The effect of six key process control parameters on the surface roughness, dimensional accuracy, and porosity in material extrusion 3D printing of polylactic acid: prediction models and optimization supported by robust design analysis. *Adv Ind Manuf Eng.* 2022;5:5. doi:10.1016/j.aime.2022.100104
30. Vidakis N, David C, Petousis M, Sagris D, Mountakis N. Optimization of key quality indicators in material extrusion 3D printing of acrylonitrile butadiene styrene: the impact of critical process control parameters on the surface roughness, dimensional accuracy, and porosity. *Mater Today Commun.* 2023;34:105171. doi:10.1016/j.mtcomm.2022.105171
31. Mushtaq RT, Wang Y, Bao C, et al. Maximizing performance and efficiency in 3D printing of polylactic acid biomaterials: unveiling of microstructural morphology, and implications of process parameters and modeling of the mechanical strength, surface roughness, print time, and print energy for fused filament fabricated (FFF) bioparts. *Int J Biol Macromol.* 2024;259:129201. doi:10.1016/j.ijbiomac.2024.129201
32. Chevali VS, Nerenz BA, Ulven CA, Kandare E. Mechanical properties of hybrid lignocellulosic fiber-filled acrylonitrile butadiene styrene (ABS) biocomposites. *Polym-Plast Technol Eng.* 2015;54(4):375-382. doi:10.1080/03602559.2014.961078
33. Sola A, Chong WJ, Pejak Simunec D, et al. Open challenges in tensile testing of additively manufactured polymers: a literature survey and a case study in fused filament fabrication. *Polym Test.* 2023;117:117. doi:10.1016/j.polymertesting.2022.107859
34. Zhao X, Tekinalp H, Meng X, et al. Poplar as biofiber reinforcement in composites for large-scale 3D printing. *ACS Appl Bio Mater.* 2019;2(10):4557-4570. doi:10.1021/acsabm.9b00675
35. Tisserat B, Joshee N, Mahapatra AK, Selling GW, Finkenstadt VL. Physical and mechanical properties of extruded poly(lactic acid)-based *Paulownia elongata* biocomposites. *Ind Crop Prod.* 2013;44:88-96. doi:10.1016/j.indcrop.2012.10.030
36. Yiga VA, Lubwama M, Olupot PW. Thermal stability of NaOH modified rice husk fiber-reinforced polylactic acid composites: effect of rice husks and clay loading. *Results Mater.* 2023;18:18. doi:10.1016/j.rinma.2023.100398
37. Rodovalho AJRL, Barbosa WT, Vieira JL, et al. Influence of size and crystallinity of nanohydroxyapatite (nHA) particles on the properties of polylactic acid/nHA nanocomposite scaffolds produced by 3D printing. *J Mater Res Technol.* 2024;30:3101-3111. doi:10.1016/j.jmrt.2024.04.048
38. Liu W, Wang Y, Xiang S, Liu H. Unveiling the effect of enhanced interfacial compatibility on the mechanical properties of PLA/PBAT blends. *Polymer.* 2024;296:126815. doi:10.1016/j.polymer.2024.126815
39. Hristov V, Vlachopoulos J. Effects of polymer molecular weight and filler particle size on flow behavior of wood polymer composites. *Polym Compos.* 2008;29(8):831-839. doi:10.1002/pc.20455
40. Magalhães Da Silva SP, Lima PS, Oliveira JM. Rheological behaviour of cork-polymer composites for injection moulding. *Compos Part B: Eng.* 2016;90:172-178. doi:10.1016/j.compositesb.2015.12.015
41. Nagarajan V, Mohanty AK, Misra M. Biocomposites with size-fractionated biocarbon: influence of the microstructure on macroscopic properties. *ACS Omega.* 2016;1(4):636-647. doi:10.1021/acsoomega.6b00175
42. Yakubu MK, Gumel MS, Umar A, Metelerkamp R. Physico-mechanical effects of surface-modified sorgum stalk powder on reinforced rubber. *J Reinf Plast Compos.* 2010;29(18):2855-2868. doi:10.1177/0731684409358470
43. Petchwattana N, Covavisaruch S. Effects of Rice Hull particle size and content on the mechanical properties and visual appearance of wood plastic composites prepared from poly(vinyl chloride). *J Bionic Eng.* 2013;10(1):110-117. doi:10.1016/S1672-6529(13)60205-X
44. du Plessis A. Effects of process parameters on porosity in laser powder bed fusion revealed by x-ray tomography. *Addit Manuf.* 2019;30:30. doi:10.1016/j.addma.2019.100871

How to cite this article: Xiao X, Chevali VS, Song P, et al. Mechanical properties and microstructure of hemp hurd reinforced polylactide biocomposites for 3D printing. *Polym Compos.* 2025;46(6):4927-4937. doi:10.1002/pc.28893